Oxidation of Porous Stainless Steel Supports for Metal-Supported Solid Oxide Fuel Cells

Michael Reisert[1], Viktoriya Berova[2], Ashish Aphale[1], Prabhakar Singh[1], Michael C. Tucker[2*]

1. Materials Science and Engineering, University of Connecticut, Storrs, CT 06269
2. Energy Conversion Group, Lawrence Berkeley National Laboratory, Berkeley, CA 94720

Abstract

Oxidation behavior of porous P434L ferritic stainless steel, used for the fabrication of metal-supported solid oxide fuel cells (MS-SOFC), is studied under anodic and cathodic atmospheres. Temperature- and atmosphere-dependence is determined for as-sintered and pre-oxidized stainless steel. Pre-oxidation reduced the long-term oxidation rate. For pre-oxidized samples, the oxidation rate in air exceeds that in humid hydrogen for temperatures above 700°C. The influence of PrOx, LSCF-SDC, and Ni-SDC coatings is also examined. The coatings do not dramatically impact oxide scale growth. Oxidation in C-free and C-containing anodic atmospheres is similar. Addition of CO_2, CH_4, and CO to humidified hydrogen to simulate ethanol reformate does not significantly impact oxidation behavior. Cr transpiration in humid air is greatly reduced by the PrOx coating, and a $PrCrO_3$ reaction product is observed throughout the porous structure. A dense and protective chromia-based scale forms on steel samples during oxidation in all conditions. A thin silica enriched oxide layer also forms at the metal-scale interface. In general, the oxidation behavior at 700°C is found to be acceptable.

Metal-supported; SOFC; oxidation; stainless steel

*mctucker@lbl.gov

Phone 1-510-486-5304

Fax 1-510-486-4260

LBNL; 1 Cyclotron Rd; MS 62-203; Berkeley CA 94720; USA

Introduction

Metal-supported solid oxide fuel cells (MS-SOFCs) and electrolysis cells (MS-SOECs) are being developed as an alternative to conventional SOFCs (electrolyte (ESC), anode (ASC), or cathode (CSC) supported cells) as the MS-SOFCs with porous stainless steel supports offer advantages including tolerance to very rapid start-up and large thermal gradients, low materials cost of the support, mechanical ruggedness, tolerance to deep redox cycling of the anode, and the possibility of metal-to-metal seals and electrical contacts produced by brazing or welding [1-4]. Introducing stainless steel to the SOFC cell materials set, however, imposes limitations to the cell and stack fabrication processes as well as operating conditions. In particular, high temperature fabrication steps, such as co-sintering of the metal support and electrolyte, must be carried out in reducing atmosphere to avoid rapid oxidation of the porous stainless steel support. Long-term oxidation is also a concern during MS-SOFC operation as the oxygen partial pressure is high enough in both the air and fuel sides to promote growth of a Cr-containing oxide scale at typical operating temperatures of 500 to 800 °C. While growth of the Cr-containing scale is ideally limited to the parabolic rate due to diffusion control and the low oxygen diffusivity in the scale, the low electronic conductivity scale adds significant impedance to the electron conduction pathways during long-term operation. Eventually, a thick scale can spall (cracking and flaking off) exposing fresh steel surface to further oxidation. These issues have been studied extensively for dense stainless steel interconnect materials, and are expected to be more problematic for porous stainless steel supports due to the higher surface-to-volume ratio and difficulty of applying state-of-the-art oxidation-resistant coatings deep into the porous structure.

Ferritic stainless steels have been conventionally used as the standard material of choice for MS-SOFC supports as they offer acceptable oxidation rate below about 750 °C, remain less expensive when compared to oxidation-resistant alloys such as Hastelloy and Inconel, and show coefficient of thermal expansion (CTE) in the range 10.4 to 11.4 ppm/K [5], matched with the CTE of standard zirconia-based electrolytes. A range of specific ferritic stainless steel alloy compositions have been successfully used as supports for MS-SOFCs, including 430, 434, and Cr26-Fe ITM [6-8].

Oxidation of porous stainless steels in conditions relevant to SOFC operation has been studied for more than a decade. The oxidation rate is sensitive to exposure temperature, alloy composition, and porosity of the substrate, with higher porosity producing higher mass gain based on the superficial surface area [9]. The oxidation rate for porous stainless steels and individual particles are similar to that of dense steel samples, suggesting that surface shape does not significantly impact oxidation rate [10, 11]. Similarly to dense stainless steels, after a brief initial rapid linear oxidation period, parabolic growth kinetics are observed, with growth of a protective oxide scale typically containing Cr_2O_3 or $MnCr_2O_4$ associated with a moderate increase in area-specific resistance (ASR) [9, 12]. An additional complication for porous materials is the growth of the scale into the pore space, which can close off pores thereby degrading gas transport pathways through the support [9, 12, 13].

The deposition of coatings throughout the porous structure improved the oxidation rate in both air and fuel atmospheres in the temperature range of 600 to 900 °C. Coating with Y, La, $La_{0.2}Sr_{0.8}Ti_{0.9}Ni_{0.1}O_{3-\delta}$ (LSTN), La(Mn,Co)-oxide (LMC), Mn-oxide, or $LaCrO_3$ [10, 14-20] decreased mass gain rate by approximately 80%. LMC decreased mass gain by three orders of

magnitude during exposure to humidified hydrogen at 600 °C - a condition at which the uncoated baseline alloy displayed breakaway oxidation [20]. Sintered stainless steels have also been pre-oxidized to form a continuous protective scale before or during coating application. The surface of pristine sintered stainless steel is hydrophobic [17]; pre-oxidation converts the surface to a hydrophilic oxide, which assists in uniformly covering the interior surface in the case of aqueous coating precursor solutions. Pre-oxidation with no additional coating is also effective in reducing the oxidation rate [20], presumably due to the formation of a continuous protective scale at high processing temperatures that persists at the operating conditions.

The parabolic growth rate constants are straightforward to determine and calculate for dense stainless steel samples. Determining the kinetic rate constants for porous stainless steels is, however, notoriously difficult. The internal area of the porous structure is much higher than the superficial area of the specimen geometry, yet is difficult to measure and evolves as the interior of the specimen oxidizes. A number of authors calculate the oxidation rate based on superficial area to avoid this complication [9, 21-23], although such rate constants are difficult to compare across specimens with different internal area or to well-established rate constants in the dense interconnect literature. Others measure internal surface area in an attempt to measure the true area-specific rate constant [10], but internal area measurements are prone to inaccuracy and vary considerably depending on the method used (i.e. Brunauer–Emmett–Teller (BET) adsoprtion, mercury-intrusion, flow permeametry, etc). Post-oxidation determination of scale thickness by scanning electron microscopy is a plausible way to directly measure accumulated oxidation, but the thickness observed depends on the relative angle between the cross-section cut and the local steel surface. The simplest widely-used approach is to report mass gain percentage (or based on

superficial area) as a function of exposure time [9, 14-16, 18-20]. This approach is useful for comparative purposes, and we employ it here.

Long-standing MS-SOFC development at Lawrence Berkeley National Laboratory (LBNL) has utilized P434L alloy, chosen for its commercial availability in water-atomized form, low cost, and shrinkage match to yttria-stabilized zirconia (YSZ) and scandia-stabilized zirconia (ScSZ) which enables effective co-sintering of the support and ceramic active layers. In contrast to most MS-SOFC designs that have the metal support on the fuel side, the LBNL design utilizes porous stainless steel as a support and current collector on both the air and fuel sides. This enables welded electrical connections and excellent current collection on both sides, and exceptional tolerance to thermal stress as demonstrated by repeated cycling from room temperature to operating temperature within 10 seconds in direct flame configuration [24, 25]. Furthermore, the symmetric structure prevents cell warping during sintering and thermal excursions, even if the shrinkage rate or coefficient of thermal expansion (CTE) are not perfectly matched between the ceramic and metal layers.

With porous stainless steel on both sides of the cell, oxidation behavior in both air and fuel atmospheres is clearly of interest. Oxidation behavior may vary between wet hydrogen and carbon-containing fuel environments relevant to reformed hydrocarbon fuels [26, 27]. Cr evaporation rate on the air side remains of significant importance, as the metal support is a source of Cr contamination for the adjacent cathode layer. In this paper, we characterize the oxidation rate of sintered porous P434L alloy in air and wet hydrogen over a range of temperatures, and determine Cr evaporation rate in air and oxidation behavior in anodic and carbon-containing simulated

reformed ethanol fuel at a nominal operating temperature of 700 °C. During cell fabrication, the supports are optionally pre-oxidized to form a continuous Cr-containing scale, and infiltration of catalysts through the stainless steel supports into the buried ceramic electrode layers naturally coats the support with the catalyst composition [13]. The impact of infiltrated catalyst coatings and pre-oxidation on the oxidation and Cr evaporation rates is therefore also assessed.

Experimental

Sample preparation

P434L porous stainless steel substrates with the composition listed in Table 1 were prepared by tapecasting and sintering at 1350°C for 2 h in 2% H_2/98% Ar. Sample shrinkage of 26% occurred during sintering. Substrates of roughly 1 cm x 1 cm were pre-oxidized in air at 850 °C for 10 h for use in anodic oxidation behavior testing. Substrates of roughly 2.5 cm x 2.5 cm were pre-oxidized for use in Cr evaporation studies and oxidation behavior in cathodic conditions to increase the total Cr transpiration. SEM analysis was conducted on regions near the center of the substrates to minimize edge effects. Select pre-oxidized samples were then coated with either 3 cycles of Pr_6O_{11-x} (PrOx) or $La_{0.6}Sr_{0.4}Co_{0.2}Fe_{0.8}O_3/Ce_{0.8}Sm_{0.2}O_2$ (LSCF-SDC), or 4 cycles of $Ni/Ce_{0.8}Sm_{0.2}O_2$ (Ni-SDC) via infiltration in air followed by catalyst coarsening at 750 °C in air for PrOx and LSCF-SDC and in 97% H_2/3% H_2O for Ni-SDC, according to procedures described in detail elsewhere [13, 28]. In certain cases, “as-sintered” substrates with no coating and no pre-oxidation were used as baseline material. Throughout the text, “fresh” is used to indicate a sample that may be pre-oxidized, coated, and coarsened, but not yet exposed to the long-term oxidation conditions.

Fe	Cr	Mo	Si	Mn	P	C	S
Bal.	16.66	0.94	0.85	0.14	0.016	0.012	0.006

Table 1. Composition of P434L ferritic stainless steel (Ametek Specialty Metal Products).

Section	Sample	Preparation	Atmosphere
1, 3	As-Sintered	Sintered only	Cathodic: Ambient air or Air/ H_2O
1, 2, 3	Pre-oxidized	Pre-oxidized (850°C 10h in air)	Anodic: 2.8% H_2, 3.4%H_2O, Bal-Ar
2, 3	Ni-SDC	Pre-oxidized and Ni-SDC coated	Anodic: 2.8% H_2, 3.4%H_2O, Bal-Ar
2, 3	PrOx	Pre-oxidized and PrOx coated	Cathodic: Ambient air or Air/ H_2O
2	LSCF-SDC	Pre-oxidized and LSCF-SDC coated	Cathodic: Ambient air
4	Uncoated	Pre-oxidized only	Anodic C-free: 52.3% H_2, 25% H_2O, bal. Ar
	Ni-SDC	Pre-oxidized and Ni-SDC coated	Anodic C-containing: 52.3% H_2, 25% H_2O, 1% CH_4, 11.8% CO, 9.9% CO_2
5	Uncoated	Pre-oxidized only	
	LSCF-SDC	Pre-oxidized and LSCF-SDC coated	Cathodic: 97% dry air, 3% H_2O
	PrOx	Pre-oxidized and PrOx coated	

Table 2. Experimental matrix for oxidation behavior and Cr evaporation studies.

Characterization

Surface morphologies of fresh samples were first characterized by scanning electron microscopy (SEM) using a FEI Quanta™ 250 FEG field emission scanning electron microscope (Thermo Scientific™) equipped with an energy dispersive x-ray spectrometer (EDS). Phase identification of the surface oxide scales was performed using a Bruker AXS D-8 Advance X-ray diffractometer (XRD) with Cu Kα radiation ($\lambda = 1.5406$ Å). A fresh coupon sample was placed on a sample holder

to acquire the data. The data was acquired over an angular range $10° < 2\theta < 90°$ with a scan step of 0.02°. Elemental analyses were performed using transmission electron microscopy (TEM) (JEOL JEM-2010 FasTEM) and samples for TEM were prepared using Focused Ion Beam (FIB) (FEI Strata 400s Dual Beam FIB), combined with a scanning electron beam and ion beam to prepare a sample for elemental analysis.

Oxidation in ambient air and humidified hydrogen

The experimental matrix outlining samples used for oxidation behavior and Cr evaporation in the different atmospheres is shown in Table 2. Initial experiments focused on the temperature-dependence and atmosphere-dependence of the oxidation behavior for as-sintered, pre-oxidized, and coated samples (Sections 1-3). The tube furnace set-up used for controlled atmospheres is shown in Fig. S1. The 2.5 cm x 2.5 cm samples (as-sintered, pre-oxidized, Ni-SDC and LSCF-SDC) were placed vertically in an alumina sample holder in the middle of a horizontal alumina tube furnace. The open end of the alumina tube was sealed with a metal flange which also serves as a connector to the inlet and outlet gas lines. The desired steam content was adjusted by bubbling the incoming gas (2.8 % H_2 in Ar, or air) through a distilled water bottle submerged in an oil bath at the required dew point temperature. The exit of this bubbler was connected to the sample chamber by a heated Teflon tube to prevent condensation. The humidified gas was further transported through an alumina gas inlet tube to the end of the alumina tube and simultaneously heated up to operating temperature. The sample chamber gas outlet line was connected to a silicon oil bubbler to prevent backflow of air into the sample chamber, and as a visual confirmation of chamber sealing. The flow rate of the dry gases was 100 sccm. The ramping rate for heating was 10 °C/min and for cooling 40°C/min. The tube furnace was calibrated prior to use and the deviation

of target temperature was less than 10 °C over the sample area. A box furnace was used for ambient air (~1.4 % H_2O). The samples were placed horizontally on porous alumina plates centrally in the box furnace. The furnaces were calibrated prior use.

To measure the weight change, oxidation was interrupted after various time intervals by cooling the furnace to room temperature, weighing the samples, and re-heating to oxidation temperature. The relatively short ramp steps were not included in the cumulative exposure time. The metal supports were dried at 100 °C for 1 h before weight measurement to remove water from the porous surface. A Mettler Toledo XP205 analytical balance was used with a 0.01 mg accuracy. The samples were weighed at least two times to obtain an average weight change value and two or three identical samples were used to ensure reproducibility. The weight change is expressed as a percentage and was calculated by comparing mass *m* after designated oxidation time with initial mass m_0 with following equation:

$$\Delta m = \frac{m - m_0}{m_0} * 100\%$$

Oxidation in C-free and C-containing simulated reformate

Further oxidation studies (Section 4) utilized a gas mix intended to simulate ethanol/water 45/55v% blend fully reformed at 700°C [29]. A C-free mixture with the same hydrogen and water content, but all C-species replaced with Ar was also used to isolate the effect of the presence of carbon. The set-up used for sample exposure to the anodic reducing atmospheres is pictured in Fig. S2. During each test (one 500 h test with C-free, one 500 h test with C-containing atmosphere), two samples each of Uncoated and Ni-SDC were placed in an alumina crucible, resting at an angle so both sides of the samples were exposed to the flowing gas atmosphere. The alumina crucible

was placed in the center of a quartz tube within a tubular furnace (STF1200, Across International). One side of the quartz tube, which sat outside of the heating zone, was used as the gas inlet. A quartz tube to 1/4" tube metal flange adaptor was used to seal the end of the quartz tube and connect it to the respective gas lines for both atmospheres. Flexible steel tubing connected the pertinent gas cylinders (Airgas) to a bubbler wrapped with a heating tape. A thermocouple inserted into the bubbler was connected to a temperature controller (Omega) which was used to heat the water to 65 °C to achieve 25% H_2O. Another flexible line was used to connect the bubbler outlet to the metal flange adaptor. This line was also wrapped with a heated tape which was set to 90 °C to ensure the temperature of the line was sufficiently high to prevent condensation of water prior to reaching the heating zone of the furnace.

A relative humidity meter (Omega) was placed within the inlet line using an adaptor and the humidity was recorded to ensure water was not condensing (i.e. 25% absolute humidity of the inlet gas was achieved). This was recorded for an hour with an inert inlet gas (N_2) to ensure the set-up was calibrated and the target humidity was achieved within the gas line to the heating zone. Before testing, the humidity sensor was removed from the line to ensure more uniform heating of the line to the heating zone and to protect the sensor from exposure to the anodic testing atmospheres.

In order to achieve the desired composition of gases, individual hydrogen/carbon dioxide/methane mix, nitrogen, and carbon monoxide streams were mixed with volume flow rates calibrated to equate to a combined 75 sccm at the bubbler inlet using mass flow controllers (MFCs). Gas cylinder compositions were normalized to 75% to account for 25% H_2O added using the bubbler. For the C-free baseline anodic atmosphere with no carbon, the hydrogen/carbon dioxide/methane cylinder was swapped for a 70% H_2 – 30% Ar cylinder. N_2 was used to purge the bubbler and

quartz tube after every test stoppage/sample weighing to ensure no CO entered the ambient lab space.

Cr evaporation

Cr evaporation (Section 5) from uncoated, and LSCF-SDC and PrOx coated P434L alloy was measured using the Cr transpiration test setup as shown in Fig. S3. A quartz tube, designed with a capillary opening to prevent the back diffusion of the vapor species, was used to conduct the experiment. Experimental test conditions simulated SOFC cathodic atmosphere of 3% H_2O/97% air at 700 °C. The surface area of the pre-oxidized samples measured using BET was 0.025 m^2/g. Care was taken during handling of the samples to avoid any possible flaking of the surface coating. Initial weight was measured and recorded before the start of the experiment using a micro-balance with an accuracy of 0.1 mg. The coupons were placed in the furnace and heated to 700 °C with a ramp rate of 5 °C min^{-1}. The furnace was calibrated before starting the experiment, using a K-type thermocouple and a constant temperature zone was determined. Cr evaporation tests were conducted for 500 h in the presence of 3% H_2O/97% air flowing at 300 sccm. After terminating the test, the temperature was brought down to room temperature (RT) at 5 °C /min, only after which the air flow was stopped and samples were removed for further analysis.

Visual observations of the outlet glass elbow were recorded to examine the extent of Cr evaporation from each sample, which normally leads to yellowish discoloration of the glass. Inductively coupled plasma-optical emission spectroscopy (ICP-OES) was performed to analyze the chromium concentration and calculate the total Cr evaporation rate. The deposited Cr on the quartz tube, elbow and the condenser was extracted by dissolving it in aqueous 20% HNO_3. Any undissolved Cr species were further removed from the glass wall by dissolving in alkaline

potassium permanganate (0.3% $KMnO_4$ in 1% NaOH, upon heating at 80 °C), ensuring the conversion of the remaining Cr species from Cr^{3+} to Cr^{6+}. For each sample type, the Cr weight determined from 3 ICP runs was averaged.

Results and Discussion

The general oxidation behavior of porous P434L with and without catalyst coatings was observed in ambient air and humidified hydrogen over a wide range of temperature in Sections 1 and 2. The results guided selection of specific conditions for more detailed study. Breakaway oxidation was observed at 600°C, so this phenomenon was explored in more detail in Section 3. Oxidation in a simulated reformate fuel environment was studied in the presence and absence of carbon-containing species in Section 4. The impact of the coatings on Cr evaporation was also determined in Section 5. Detailed observation of the oxide scale was undertaken for selected conditions.

1. Oxidation atmosphere and temperature

The oxidation rate for stainless steel is impacted by many factors, including: alloy composition, coating composition, thickness and porosity, and oxidation temperature and exposure atmosphere chemistry. Ambient air and hydrogen/steam/argon mixture with hydrogen:steam ratio of 45:55 were chosen to represent cathode and anode environments in a SOFC, respectively. The oxidation rate is strongly dependent on temperature, as evident in Fig. 1. The expected parabolic oxidation kinetics are observed for hydrogen/steam exposure condition at 700 °C and for air at 750 °C and above (Fig. 1a). Exposure to lower temperatures (650 °C and below) in air led to non-parabolic weight gain or weight loss. Observed previously, such weight changes are attributed to competition

between weight gain due to oxidation and weight loss due to Cr evaporation, with Cr evaporation dominating at lower temperature [30].

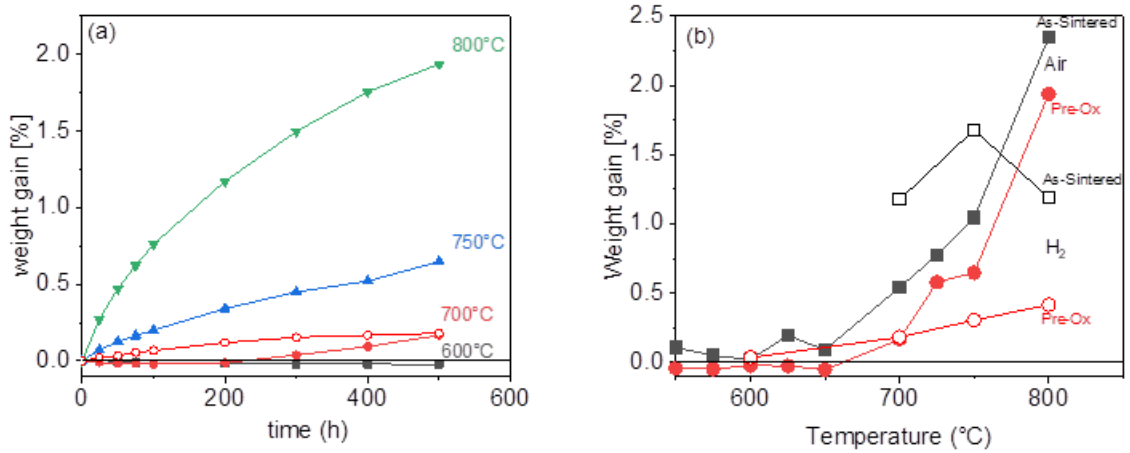

Figure 1. Impact of temperature, atmosphere, and pre-oxidation on oxidation behavior. Ambient air (filled markers), hydrogen/steam (open markers). (a) Time dependence of weight gain for pre-oxidized coupons at various temperatures. (b) Temperature-dependence of weight gain at 500 h of as-sintered (squares) and pre-oxidized uncoated (circles) coupons.

The influence of temperature, atmosphere, and pre-oxidation on weight change is summarized in Fig. 1b. For air, the steep increase in weight gain with temperature above 650 °C is consistent with the Arrhenius dependence reported for oxidation rate of stainless steel powder [11]. The anomalous trend for as-sintered alloy in hydrogen/steam is likely due to imperfect steam content control, which was improved for later experiments. Pre-oxidation at 850°C, which is currently a standard processing step prior to catalyst infiltration [13], reduces oxidation rate moderately in ambient air and significantly in humidified hydrogen. The thick, continuous oxide scale formed at 850 °C is more protective than the thin scale formed in-situ at short times and lower temperatures. Oxidation rates for the pre-oxidized alloy are similar for air and hydrogen/steam for 700 °C and

lower, but oxidation in air is significantly more rapid at higher temperature. High weight gain due to breakaway oxidation at 600 °C for as-sintered stainless steel in hydrogen/steam is not shown, but is discussed in detail below in Section 3.

Determining oxidation rate for porous samples is notoriously difficult, as discussed above in the Introduction. Two methods for estimating the oxidation rate were used here: based on the 0.2 to 0.5 μm thickness of the oxide scale observed with SEM after oxidation (Fig. S12); or, calculated from the weight gain and approximate internal surface area of as-sintered specimens before oxidation. These estimates are consistent with the range reported previously for similar stainless steel compositions, Table 3, and with the 0.9 μm scale thickness observed previously for a MS-SOFC operated for 1200 h at 700 °C [31]. We speculate that the value based on scale thickness is more accurate because it is based on a direct measurement taken at the end of the oxidation period, whereas the BET surface area is determined before oxidation occurs, and it is expected that the surface area will change during oxidation as the surface morphology changes due to scale growth.

Reference	Alloy	Atmosphere	Oxidation rate (g^2 cm^{-4} s^{-1})	Note
[32]	430	Air	2×10^{-16} to 2×10^{-15}	Various porosities
[11]	430	Air	2.17×10^{-15}	Unsintered particles
[18]	430	Air	2.53×10^{-15}	Mott filter
[16]	20.6% Cr	Air	8×10^{-15}	Hoganas alloy
This work	434	Air	2.4×10^{-16}	Based on BET surface area
This work	434	Hydrogen/steam	1.1×10^{-15}	Based on BET surface area
This work	434	Air, Hydrogen/steam	1×10^{-15} to 5×10^{-15}	Based on scale thickness

Table 3. Oxidation rate at 700 °C for as-sintered porous ferritic stainless steels.

2. Impact of catalyst coatings

Infiltration of catalyst precursor through the metal support and into the buried electrode layer naturally coats the metal support with porous catalyst. The impact of this coating on oxidation behavior is of interest. The standard catalyst coatings used at LBNL are Ni-SDC for the fuel side, and PrOx or LSCF-SDC for the oxygen side [28, 33, 34]. The presence of coatings does not change the general trend that oxidation in air and fuel are similar around 700°C, but at higher temperature the air-side oxidation prevails and is therefore expected to contribute more to degradation of the MS-SOFC, Fig. 2. In hydrogen/steam, the Ni-SDC coating moderately reduces the extent of oxidation throughout the range 700 to 800°C. The behavior in ambient air is more complex. The weight gain cannot be directly assigned to Cr-containing scale oxidation, as other processes can also affect the sample weight, including localized iron oxidation, evaporation of Cr or other elements, segregation of elements within the coating, and reaction between the coating and substrate or vapor species. For LSCF-SDC, the coating reduces weight gain at 700°C, but moderately enhances weight gain at higher temperature. For PrOx, weight gain is moderately reduced for 750 and 800°C, but significantly increased at 700°C. We suspect that this significant weight gain for PrOx may partly be due to a limited amount of iron oxidation in addition to Cr_2O_3 scale growth, similar to the breakaway oxidation observed for lower temperature and higher humidity discussed in Section 3. It may also arise from reaction between PrOx and Cr vapor which is accompanied by weight gain due to oxygen uptake, i.e.:

$$(1) \qquad Pr_6O_{11} + 6\ Cr + 3.5\ O_2 \rightarrow 6\ PrCrO_3$$

This hypothesis is supported by additional observations discussed in Section 5. In particular, $PrCrO_3$ is detected after oxidation, and the Cr_2O_3 oxide scale thickness for uncoated, LSCF-SDC,

and PrOx samples is similar after 500 h exposure to wet air at 700°C indicating LSCF-SDC and PrOx do not greatly accelerate Cr_2O_3 formation under that condition. Similarly, a reaction between LSCF and Cr vapor may be accelerated at 750°C and higher. Regardless, the porous coatings used here are not expected to reduce oxidation rate or Cr evaporation as well as a dense coating would. Development of alternative denser coatings for porous stainless steel may be necessary, and this has already been pursued by other groups [10, 17].

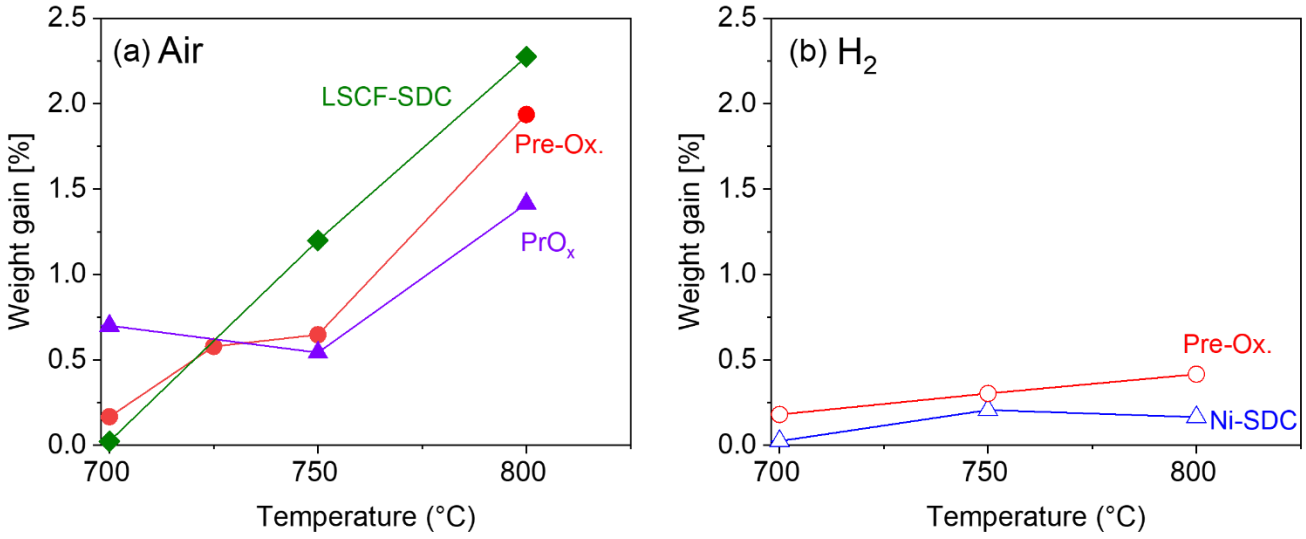

Figure 2. Impact of coatings on oxidation behavior. Temperature-dependence of weight gain at 500 h in (a) ambient air or (b) 300 h in hydrogen/steam. Coupons were pre-oxidized before applying the coating compositions listed on the figure.

3. Breakaway oxidation

Breakaway oxidation of stainless steels occurs when a protective chromia scale is not formed and rapid iron oxidation ensues. This is known to be an issue particularly around 600 °C, where Cr diffusion in the bulk is too slow to produce a protective scale [26, 35]. Breakaway oxidation is clearly observed at 600 °C for porous P434L stainless steel under certain conditions as apparent

in Fig. 3. For as-sintered alloy, breakaway does not occur in ambient air within 500 h, but does occur for higher humidity. This is a concern for operation of metal-supported solid oxide cells with porous stainless steel exposed to moist oxygen-rich environments, for example a SOFC with a leak causing steam formation in the cathode chamber, or a proton-conducting SOEC which forms a mixture of steam and oxygen as electrolysis progresses [36]. Note that the weight gain is an order of magnitude higher than observed for the normal oxidation conditions discussed in previous sections, and the pores are nearly completely filled with oxidation product, Fig. 3b. The oxidation rate is somewhat reduced at very high humidity level, presumably due to lower oxygen partial pressure. A similar trend was observed previously for oxidation of dense stainless steel interconnect alloy in air/steam mixtures with high steam content [37].

Pre-oxidation of the stainless steel at 850 °C forms a continuous scale that persists and remains protective at 600 °C within the range of humidity studied here. Low oxidation rate, and retention of the highly porous initial structure is observed, Fig. 3c. Addition of Pr-oxide coating negates the protective effect of the pre-oxidized scale, enhancing breakaway oxidation at high humidity in air. This is presumably due to consumption of Cr in the scale via reaction (1), which is discussed for other conditions in Sections 2 and 5. The PrO_x-coated specimens also expand significantly; linear expansion of ~10% for 10-25% humidity, and 63% for 50% humidity was observed. Use of a catalyst coating that does not react with chromia is expected to mitigate these issues.

In the hydrogen-containing fuel atmosphere, breakaway oxidation was observed for as-sintered alloy. Pre-oxidation suppresses breakaway oxidation, and in contrast to PrO_x coating, addition of

Ni-SDC coating does not enhance breakaway because it does not react with chromia under these conditions.

These observations help to explain our previous report of rapid failure of metal-supported SOFCs with PrO_x-coated stainless steel supports operated at 600 °C [13]. The air-side metal support displayed pore filling and delaminated from the rest of the cell. It is thought that a pinhole in the electrolyte or small leak in the seal leads to burning of hydrogen on the air side, and the resulting steam formed on the air side promotes breakaway oxidation. The physical expansion of the PrOx-coated specimens here is consistent with delamination of the air-side metal support for the full cells.

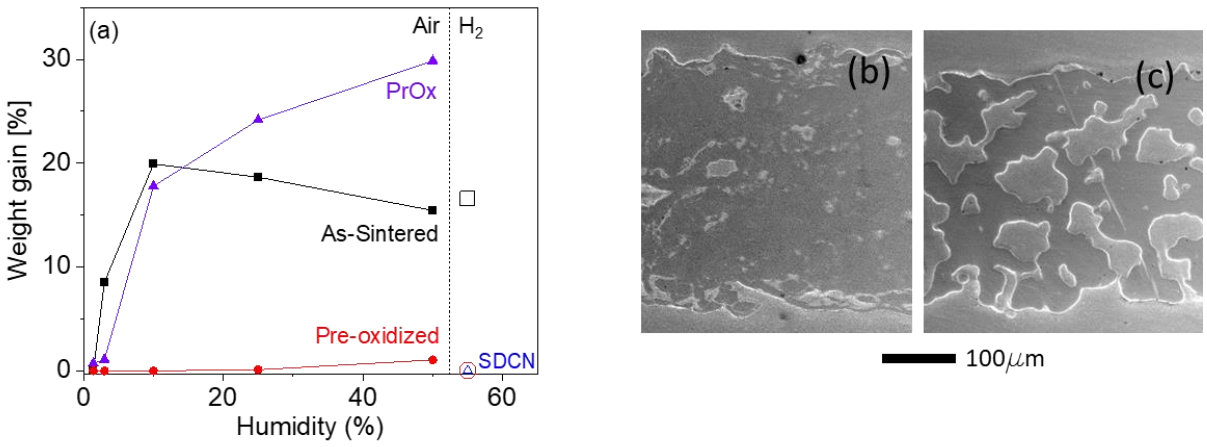

Figure 3. Breakaway oxidation at 600 °C. (a) Humidity-dependence of the weight gain after 500 h in air (filled markers) or hydrogen/steam (open markers), for as-sintered (squares), pre-oxidized (circles), or coated (triangles) coupons. PrOx-coated was exposed to air and Ni-SDC-coated was exposed to hydrogen/steam. Note that air with humidity in the range of ~1.5 to 50% was studied, but only 55% humidity was studied for hydrogen/steam. The markers for pre-oxidized and Ni-SDC samples in

hydrogen/steam overlap. SEM images of polished cross-section after oxidation for 500 h in air with 25% humidity for (b) as-sintered, and (c) pre-oxidized coupons with no coating.

4. Oxidation in fuel with and without carbon

Detailed study of oxidation in the fuel environment was undertaken to expand on the observations in Section 1. Previous research efforts have focused on electrode and catalyst behavior in fuel environments containing carbon species during the utilization of hydrocarbon fuels [38]. This study is designed to additionally understand whether C-containing fuel reformate components pose anomalous oxidation/corrosion issues in the present metal supports. MS-SOFCs are being considered as range extenders for electric vehicles, using ethanol/water blend as fuel [29]. Therefore, ethanol reformate containing multiple carbon-based gaseous products such as CH_4, CO, and CO_2 is a relevant fuel environment to consider and oxidation was studied in C-containing and C-free atmospheres. The C-free atmosphere contained the same hydrogen and steam contents, but the C-containing species were replaced with Ar.

Pre-oxidized samples with and without a Ni-SDC coating were prepared. The uncoated sample has a mostly uniform oxide scale with some anomalous orb-like structures, Fig 4. EDS revealed the pre-oxidized scale is mainly Cr_2O_3 with minor presence of Mn and Si. The anomalous orb-like structures were identified as Ti/Zr/Y oxide which deposited during sintering from the YSZ powder used to separate the green metal support from the alumina sintering plate, and stray Ti used as an oxygen getter in the furnace, and can therefore be considered an artifact of the lab-scale fabrication procedure. The entire surface of the Ni-SDC sample is coated with porous catalyst, although the thickness does not appear to be uniform.

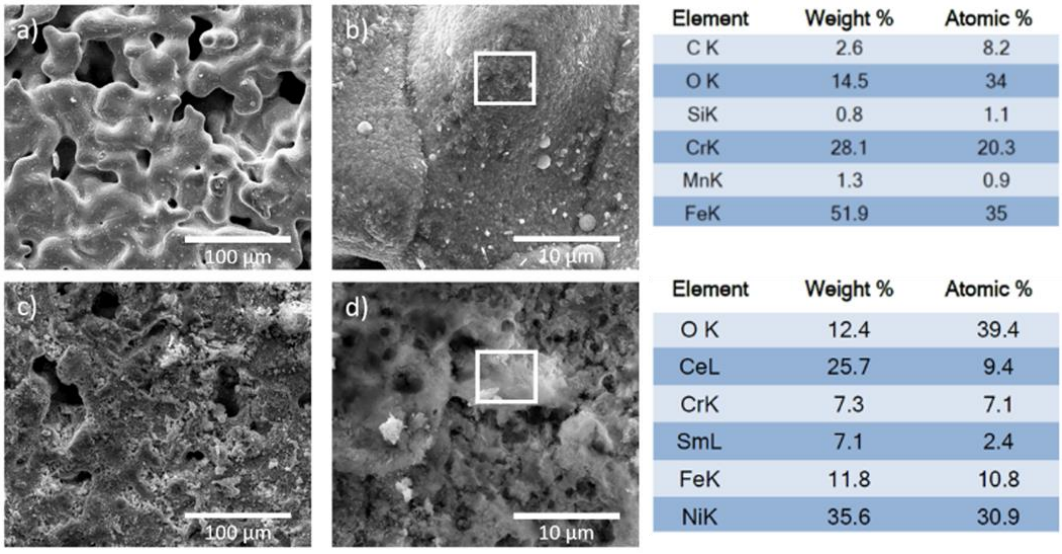

Element	Weight %	Atomic %
C K	2.6	8.2
O K	14.5	34
SiK	0.8	1.1
CrK	28.1	20.3
MnK	1.3	0.9
FeK	51.9	35

Element	Weight %	Atomic %
O K	12.4	39.4
CeL	25.7	9.4
CrK	7.3	7.1
SmL	7.1	2.4
FeK	11.8	10.8
NiK	35.6	30.9

Figure 4. Porous samples for oxidation in fuel atmosphere. SEM surface image of fresh (a,b) uncoated and (c,d) Ni-SDC samples. EDS elemental analysis corresponds to the white boxes in the adjacent SEM images.

4.1. C-free atmosphere

For the uncoated sample, after 500 h exposure to C-free atmosphere, there is no breakaway oxidation, indicative of the passivating nature of the pre-oxidized Cr-based scale. Coarsening and Si-based oxide overgrowth at the oxide scale surrounding the orb-like structures occurred, however the majority of the scale appears unaffected, Fig 5a. The uncoated sample (after 500 h of exposure) was sectioned using FIB milling and subsequently analyzed by transmission electron microscopy (TEM). A section was chosen to investigate the predominant thin scale, orb-like structures, and Si-oxide overgrowth. Elemental analysis of the orb-like structures indicate that they remain mainly Ti/Zr/Y based oxide. The uninterrupted scale adjacent to these orb-like structures is ~ 380 nm and consists of a Cr/Mn mixed oxide scale of ~ 330 nm with a thin (~ 50 nm) sublayer containing SiO_2 (Fig. S6). The effects of high humidity which can cause rapid iron oxidation are not apparent. Similarly, the oxide scale seems well-adhered and does not show signs of spallation or formation

of mixed oxide overgrowth. Si-oxide grew above a denser area of the Cr/Mn oxide, as seen near the top of the TEM images. Overall scale thickness changes can only be seen in some areas of Si-based oxide overgrowth (~ 3-4 µm from surface to top of overgrowth).

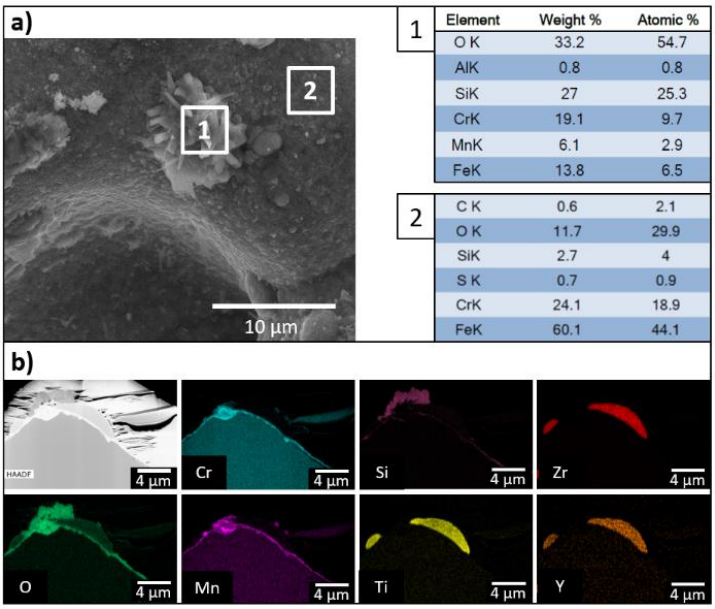

Figure 5. Oxide scale of uncoated sample after 500 h of exposure to C-free atmosphere at 700 °C. (a) SEM micrograph areas 1 and 2 correspond to the adjacent EDS elemental analysis. (b) TEM analysis of FIB-milled cross-section.

In humid atmosphere, enhanced oxidation of the alloy is postulated to be due to the dissociation of the water molecule and easy inward diffusion of OH^- which may subsequently react with Si and other metal constituents [39, 40]. Furthermore, SiO_2 is thermodynamically stable in very low pO_2 and with a H_2/H_2O ratio of 52.3/25, the partial pressure of oxygen due to the presence of water is more than sufficient to oxidize Si. The SiO_2 overgrowth does not form a continuous scale above the pre-oxidized scale, however the presence of insulating SiO_2 may cause a loss of electrical conductivity through the pre-oxidized scale. This is important to consider, as the metal support in an MS-SOFC collects current collectors from the active electrodes. Nevertheless, the excellent

durability previously demonstrated for MS-SOFCs suggests scale growth is not a significant source of ASR degradation during the hundreds of hours tested [13].

For the Ni-SDC coating, after exposure there are 1 μm and smaller Ni particles in multiple areas of the surface coating, which may be a result of Ni coarsening and segregation from the coating, Fig 6. This is not surprising, as Ni coarsening and agglomeration is a known degradation mode for MS-SOFCs with infiltrated Ni catalyst [41]. The infiltrated coating appears porous with Ni segregation seen in the pore space between metal particles of the base alloy, Fig. 6b. The same pre-oxidized scale below the Ni-SDC coating is observed here, where a Cr/Mn predominant oxide scale with a sublayer of SiO_2 is still well-adherent and stable after exposure to C-free atmosphere.

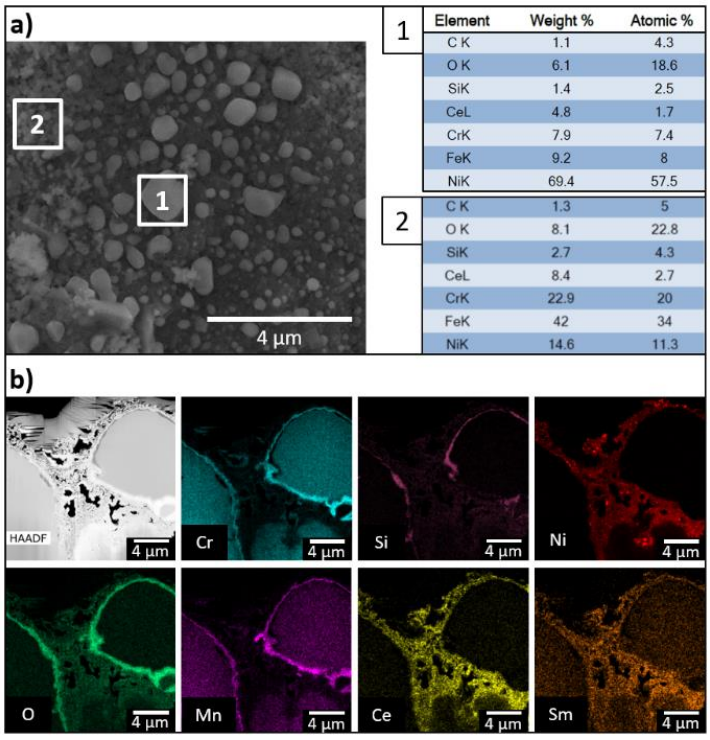

Figure 6. Oxide scale and coating for Ni-SDC sample after 500 h of exposure to C-free atmosphere at 700 °C. (a) SEM micrograph areas 1 and 2 correspond to the adjacent EDS elemental analysis. (b) TEM analysis of FIB-milled cross-section.

To compare changes in the scale chemistry and compliment EDS results, XRD analysis was performed on uncoated and Ni-SDC samples before and after exposure to C-free atmosphere for 100, 300, and 500 h, Fig. 7. Minimal changes in scale chemistry are observed for the uncoated sample. Peaks arising from Cr_2O_3 and $MnCr_2O_4$ are observed, consistent with the mixed Cr/Mn oxide scale seen in TEM analysis. While Si-based oxide formation is observed on the uncoated sample with TEM, it is not apparent from XRD analysis. The Ni-SDC sample, additionally shows formation of minor XRD peaks corresponding to Fe_2O_3 and SiO_2. We take the findings using EDS and TEM elemental mapping as a better representation of the scale chemistries before and after exposure to C-free atmosphere. However, the XRD analysis did confirm that relatively little changes in scale chemistry for both samples occur.

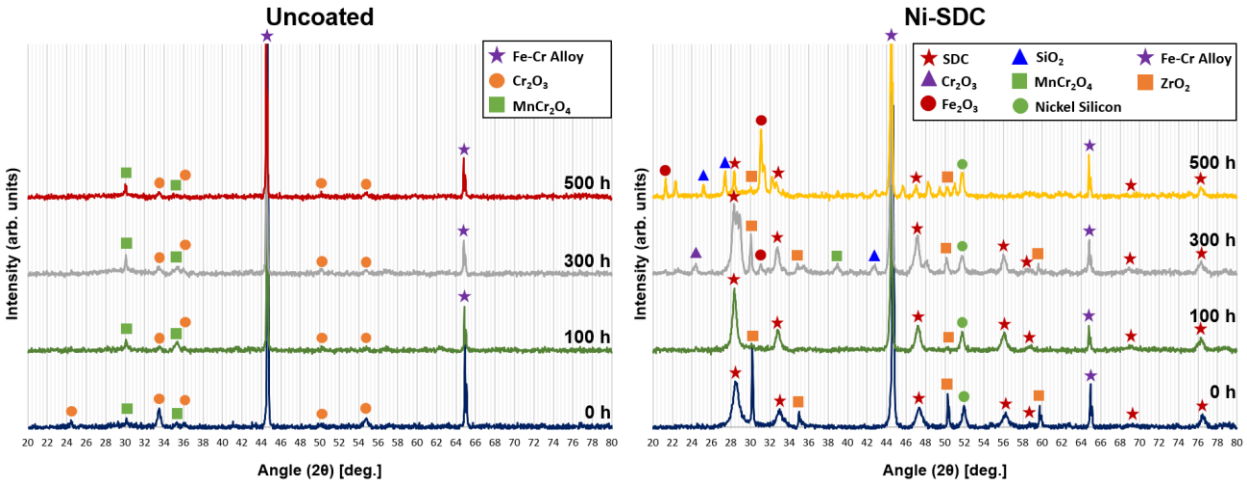

Figure 7. Surface phase XRD analysis for uncoated and Ni-SDC samples after exposure to C-free atmosphere for various times at 700 °C.

4.2. C-containing atmosphere

Introducing carbon to the anodic atmosphere did not show any appreciable effect on the observed oxidation behaviors of both uncoated and Ni-SDC samples, Fig 8. In particular, there is no solid

carbon deposition or carbon compound formation, consistent with thermodynamic predictions that the relatively high steam-to-carbon ratio used to mimic ethanol reformate atmosphere falls outside the carbon deposition region (Fig. S7). Furthermore, introducing carbon to the fuels does not appear to induce typical carbon-based surface degradation phenomena such as metal dusting, pitting corrosion, or carbide formation. This is apparent in SEM analysis of the surface of samples. The uncoated sample shows similar SiO_2 overgrowth dispersed on a relatively uniform and unchanged scale that does not reveal any high levels of carbon (Fig. S8). Similarly to C-free conditions, minor SiO_2 formation is observed and Ni-SDC shows the same Ni particulate segregation. FIB cross-sections of the uncoated and Ni-SDC samples after exposure are included within the supplemental information (Fig. S9 and Fig. S10), and confirm the behavior in C-containing and C-free atmospheres is similar.

Interestingly, the surface also shows infrequent localized formation of whisker and platelet-type oxide overgrowth, Fig. 9, considered to be a result of oxidation in high humidity [39, 42]. These areas appear to coincide with areas of Ni segregation, however they appear so rarely that a strong correlation cannot be made. TEM and EDS analysis revealed that the whisker-type oxide was a Cr/Mn-based oxide elementally similar to the oxide layer developed during the pre-oxidation process (Fig. S10). It is probable that this localized oxidation is a product of high humidity and not directly related to the presence of carbon, although SEM analysis for C-free atmosphere did not distinctly show it. Localized anomalous oxidation has been observed previously, but does not seem to impact integrity of the metal support if it remains localized [17].

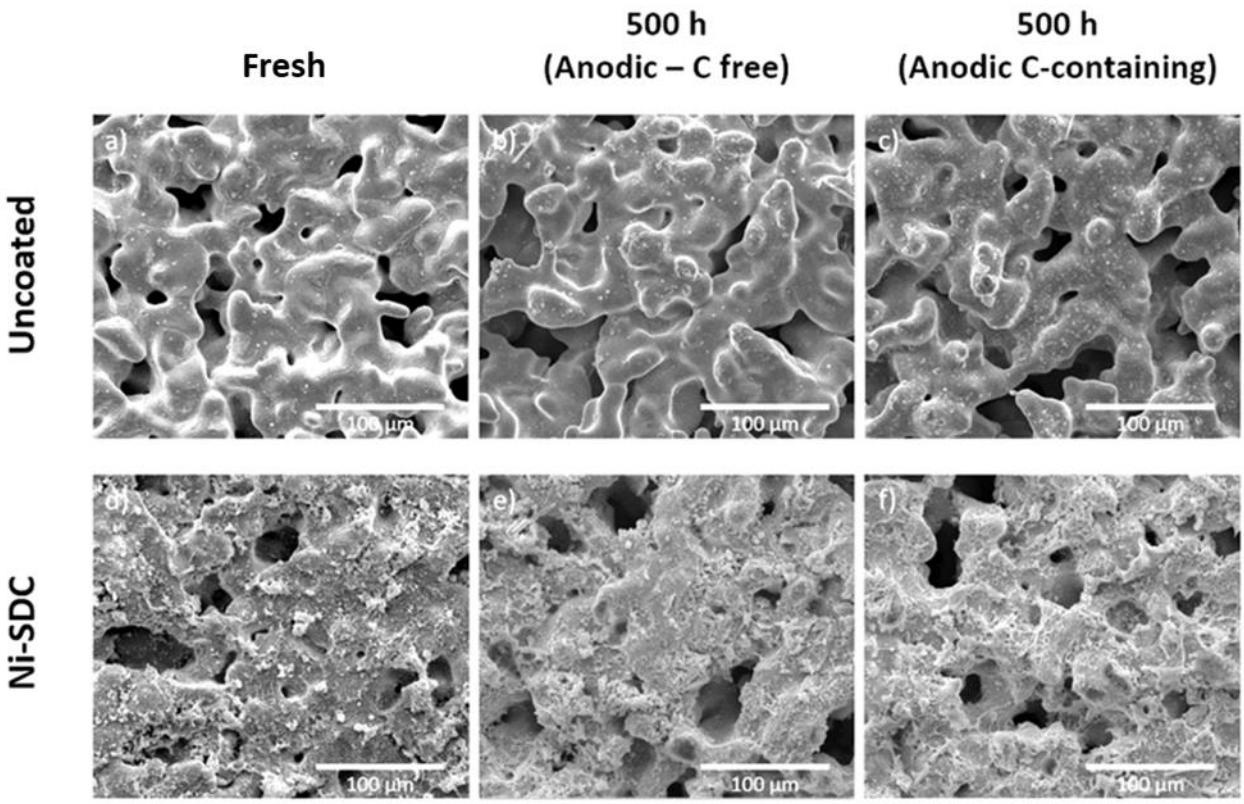

Figure 8. Comparison of porous structure of (a-c) uncoated and (d-f) Ni-SDC samples after exposure to C-free and C-containing atmosphere at 700 °C. SEM surface micrographs (a,c) before exposure and after exposure to (b,e) C-free and (c,f) C-containing anodic atmospheres.

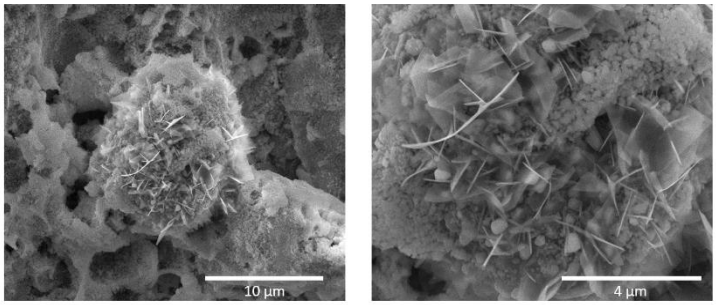

Figure 9. Anomalous isolated whisker growth. Lower magnification (left) and high magnification (right) SEM micrographs of Ni-SDC coated sample after 500 h of exposure to C-containing atmosphere at 700 °C.

5. Oxide scale formation and Cr evaporation in air

Cr evaporation from the stainless steel, and subsequent deposition onto the oxygen catalyst is a known degradation mode for MS-SOFCs and MS-SOECs with stainless steel on the air side [13, 31, 33]. Here, the impact of catalyst coatings on the Cr evaporation rate is determined over 500 h at 700°C in air with 3% H_2O. The morphology and composition of the oxide scale and catalyst coatings are also analyzed after the exposure.

The surface morphologies of each as-prepared sample are shown in Fig. 10. Pre-oxidation of P434L in air at 850 °C for 10 h produces a uniform surface oxide layer, easily observed on the uncoated sample, Fig. 10a,b. SEM-EDS (Table S1) and XRD (Fig. S12) analysis of the surface scale reveals the presence of Cr_2O_3, and SiO_2 which may be present as a sub-scale formed during pre-oxidation. The coated samples showed different surface morphologies, due to the presence of LSCF-SDC and PrOx catalyst layer coatings. The expected elements and phases are confirmed. For the PrOx sample, minor Fe-oxide and (Fe,Cr)-oxide are also detected.

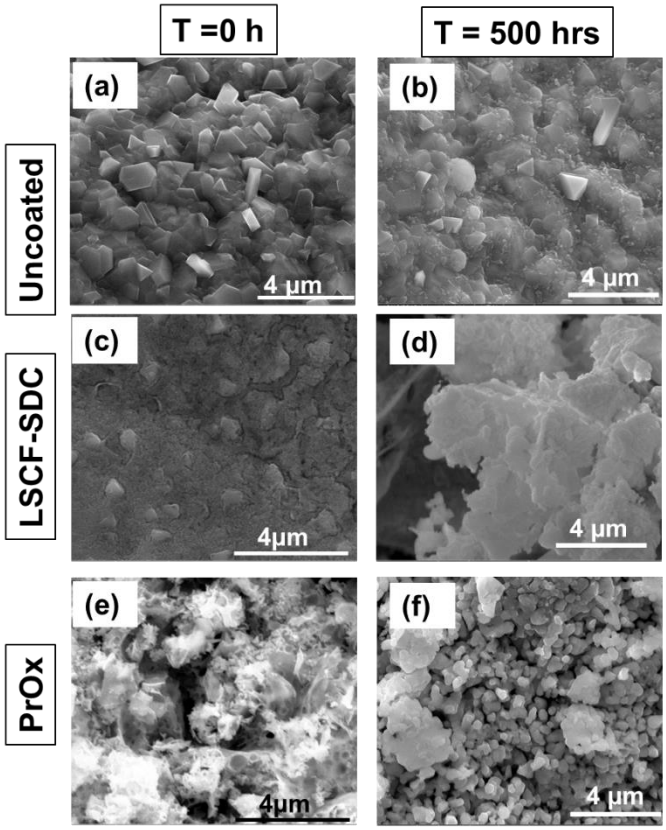

Figure 10. Oxide scale and coatings of Cr transpiration samples. SEM surface micrographs of (a,c,e) fresh and (b,d,f) exposed samples after 500 hrs of transpiration in humidified air at 700 °C. (a,b) Uncoated, (c,d) LSCF-SDC coated, and (e,f) PrOx coated samples.

The Cr evaporation rate was determined over 500 h transpiration for each of the alloy samples. Cr was collected by condensing in the outlet elbow of the furnace sample tube. Extensive discoloration of the outlet elbow is seen for the uncoated sample, with less observed for the LSCF-SDC and PrOx samples, Fig. S11. The condensed Cr was dissolved and analyzed with ICP-OES to quantify the total mass of the Cr deposited. The corresponding Cr transpiration rate was 1.75×10^{-11} kg m^{-2} s^{-1} for the uncoated sample, 7.13×10^{-12} kg m^{-2} s^{-1} for LSCF-SDC, and 2.89×10^{-12} kg m^{-2} s^{-1} for PrOx. The coatings are found to significantly suppress release of chromium vapors. PrOx is particularly effective, perhaps due to Cr consumption via reaction (1).

The surface scale morphology for the uncoated sample does not change significantly after the 500 h transpiration test; the morphology of the pre-oxidation scale remains, Fig. 10b. In contrast to this, the catalyst coatings coarsen significantly, Fig. 10d,f. This is consistent with catalyst coarsening observed previously in the electrode layer after long-term operation, which contributes to cell degradation [13, 31, 33]. SEM-EDS analysis of the surface detected a significant increase in Cr content of the PrOx coating (Table S1), consistent with the cross-section analysis discussed below.

After the Cr transpiration tests, thin sample cross sections were prepared using a FIB technique and analyzed with TEM, Fig. 11. The uncoated sample contains a uniform oxide scale about 230 to 370 nm thick, with predominantly Cr_2O_3 at the air/oxide interface. Presence of minor SiO_2 impurity is also observed. For the coated samples, a thin and dense layer of Cr_2O_3 oxide scale is observed at the metal/oxide interface, with the thick coating layers visible on the exterior. The Cr_2O_3 scale thickness was 350-440 nm for LSCF-SDC, and 240-530 nm for PrOx, Fig. S14. Note that the FIB cut is not always perpendicular to the steel/Cr_2O_3 interface so these numbers may overstate the actual thickness, and should be interpreted as an upper bound on thickness. A small extent of Cr contamination of the LSCF-SDC coating is visible. The PrOx coating on the other hand shows significant reaction with Cr, resulting in formation of $PrCrO_3$ as validated by XRD, Fig. S13. While this consumption of Cr may reduce the Cr evaporation rate in the short term, we presume that the catalyst coating will eventually become saturated with Cr and no longer provide a protective effect. This will be examined in more detail in the future.

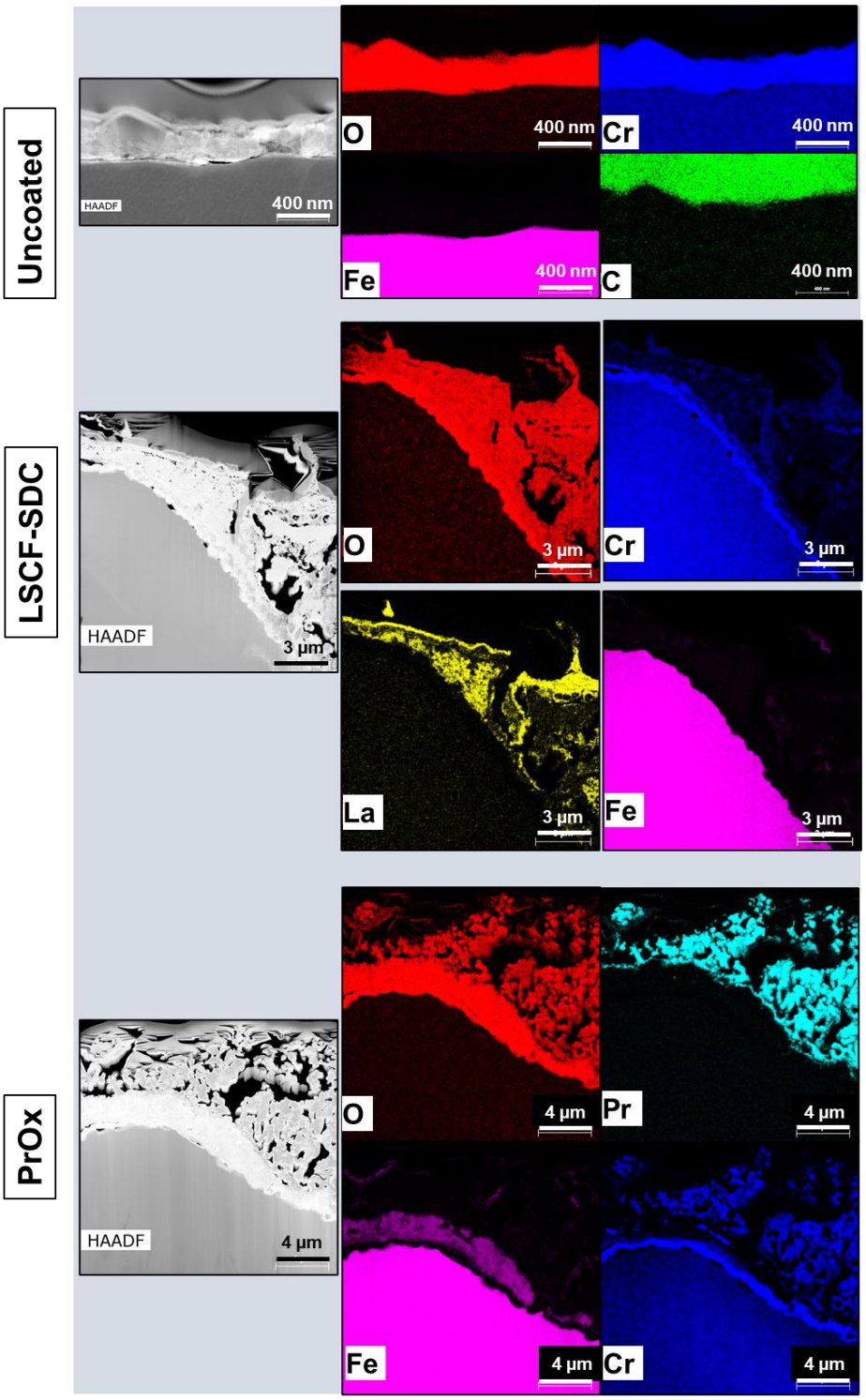

Figure 11. Scale and coatings after Cr transpiration. TEM analysis of FIB liftout sections of (top) uncoated, (middle) LSCF-SDC, and (bottom) PrOx samples after 500h exposure to humidified air at 700 °C.

Conclusions

Oxidation and Cr transpiration behavior was studied for porous ferritic stainless steel P434L, a candidate support material for MS-SOFCs. Significant oxidation occurred at 600°C and higher, with oxidation rates estimated to be similar to previous studies of other porous ferritic stainless steel alloys. Pre-oxidation in air produced a thin, conformal and protective Cr_2O_3-based coating, which lowered the long-term oxidation rate. For pre-oxidized alloy, the oxidation rate in air and humid hydrogen was similar at 700°C, but at higher temperatures the oxidation rate was significantly higher in air. Ni-SDC coating reduced the oxidation rate in humid hydrogen moderately. LSCF-SDC and PrOx coatings did not significantly impact the oxide scale thickness formed in air, but anomalous weight gain was observed and assigned to reaction of Cr vapor with the coating. Breakaway oxidation was observed at 600°C in both humid air and humid hydrogen, leading to rapid oxidation and in some cases pore filling with oxidation products. Pre-oxidation was effective at suppressing breakaway oxidation. In air, the extent of breakaway oxidation was related to humidity level, with humidity higher than about 3% being problematic.

Most previous studies of porous stainless steel oxidation relevant to SOFCs have focused on hydrogen/steam anodic atmosphere. Here, the addition of CO_2, CH_4, and CO to simulate ethanol reformate was also considered. Direct comparison between C-free and C-containing fuel atmosphere revealed that the presence of carbon does not significantly influence the oxidation behavior. Carbon deposition was not observed, and the scale morphology was similar for both anodic atmospheres. Introducing carbon-containing reformate products to the anodic fuel atmosphere did not result in the formation of carbon, carbides or other reaction products on the sample surface. This is attributed to low carbon activity in the gas phase based on calculated C-H-

O equilibrium for the relevant reformate composition. Minimal changes in oxide scale after 500 h of anodic fuel atmosphere exposure demonstrated that the candidate material may be used in an ethanol-fueled MS-SOFC system.

Evaporation of Cr from the stainless steel was studied in humidified air. Cr transpiration rate was greatly reduced by PrOx coating, and moderately reduced by LSCF-SDC coating. The PrOx coating reacted with Cr vapor to form a thermodynamically stable $PrCrO_3$ reaction product.

In summary, the oxidation behavior of porous P434L stainless steel was found to be acceptable in cathodic atmosphere, and anodic atmospheres with both the presence and absence of carbon-based gas species. Growth of a SiO_2 scale and stability of the coatings in the presence of Cr-containing vapor deserve further attention.

Acknowledgements

The authors thank Fengu (Kris) Shen for assistance with SEM imaging. The information, data, or work presented herein was funded in part by the Advanced Research Projects Agency – Energy (ARPA-E), U.S. Department of Energy under work authorization number 18/CJ000/04/01. This work was funded in part by the U.S. Department of Energy under contract no. DE-AC02-05CH11231. University of Connecticut acknowledges the financial support from US DOE under ARPAe OPEN 2018 (DE-AR0001012). We thank Nissan Motor Co., Ltd. and Nissan Technical Center North America for providing cost share. The authors would thank University of Connecticut for providing laboratory support in a timely manner. The views and opinions of the

authors expressed herein do not necessarily state or reflect those of the United States Government or any agency thereof. Neither the United States Government nor any agency thereof, nor any of their employees, makes any warranty, expressed or implied, or assumes any legal liability or responsibility for the accuracy, completeness, or usefulness of any information, apparatus, product, or process disclosed, or represents that its use would not infringe privately owned rights.

References

[1] Dayaghi AM, Kim KJ, Kim S, Park J, Kim SJ, Park BH, et al. Stainless steel-supported solid oxide fuel cell with La 0.2 Sr 0.8 Ti 0.9 Ni 0.1 O 3−δ /yttria-stabilized zirconia composite anode. Journal of Power Sources. 2016;324:288-93.
[2] Krishnan VV. Recent developments in metal-supported solid oxide fuel cells. Wiley Interdisciplinary Reviews: Energy and Environment. 2017;6:e246.
[3] Larring Y, Fontaine M-L. Critical Issues of Metal-Supported Fuel Cell. 2013:71-93.
[4] Tucker MC. Progress in metal-supported solid oxide fuel cells: A review. Journal of Power Sources. 2010;195:4570-82.
[5] Design Guidelines for the Selection and Use of Stainless Steel: Nickel Development Institute.
[6] Thaler F, Udomsilp D, Schafbauer W, Bischof C, Fukuyama Y, Miura Y, et al. Redox stability of metal-supported fuel cells with nickel/gadolinium-doped ceria anode. Journal of Power Sources. 2019;434:226751.
[7] Tucker MC. Development of High Power Density Metal-Supported Solid Oxide Fuel Cells. Energy Technology. 2017;5:2175-81.
[8] Zhou Y, Yuan C, Chen T, Meng X, Ye X, Li J, et al. Evaluation of Ni and Ni–Ce0.8Sm0.2O2−δ (SDC) impregnated 430L anodes for metal-supported solid oxide fuel cells. Journal of Power Sources. 2014;267:117-22.
[9] Molin S, Gazda M, Jasinski P. High temperature oxidation of porous alloys for solid oxide fuel cell applications. Solid State Ionics. 2010;181:1214-20.
[10] Dayaghi AM, Kim KJ, Kim SJ, Sung YS, Choi GM. Oxidation of porous stainless-steel coated with donor-doped SrTiO3 in anodic atmosphere of solid oxide fuel cell. Journal of Power Sources. 2017;360:488-94.
[11] Karczewski J, Brylewski T, Miruszewski T, Andersen KB, Jasinski PZ, Molin S. High-temperature kinetics study of 430L steel powder oxidized in air at 600–850 °C. Corrosion Science. 2019;149:100-7.
[12] Reiss G, Frandsen HL, Persson ÅH, Weiß C, Brandstätter W. Numerical evaluation of oxide growth in metallic support microstructures of Solid Oxide Fuel Cells and its influence on mass transport. Journal of Power Sources. 2015;297:388-99.
[13] Dogdibegovic E, Wang R, Lau GY, Karimaghaloo A, Lee MH, Tucker MC. Progress in durability of metal-supported solid oxide fuel cells with infiltrated electrodes. Journal of Power Sources. 2019;437:226935.
[14] Molin S, Gazda M, Jasinski P. Coatings for improvement of high temperature corrosion resistance of porous alloys. Journal of the European Ceramic Society. 2011;31:2707-10.

[15] Stange M, Stefan E, Denonville C, Larring Y, Rørvik PM, Haugsrud R. Development of novel metal-supported proton ceramic electrolyser cell with thin film BZY15–Ni electrode and BZY15 electrolyte. International Journal of Hydrogen Energy. 2017;42:13454-62.
[16] Stefan E, Denonville C, Larring Y, Stange M, Haugsrud R. Oxidation study of porous metal substrates for metal supported proton ceramic electrolyzer cells. Corrosion Science. 2020;164:108335.
[17] Stefan E, Neagu D, Blennow Tullmar P, Persson ÅH, Sudireddy BR, Miller D, et al. Spinel-based coatings for metal supported solid oxide fuel cells. Materials Research Bulletin. 2017;89:232-44.
[18] Yan Y, Bateni R, Harris J, Kesler O. Fabrication of reactive element oxide coatings on porous ferritic stainless steel for use in metal-supported solid oxide fuel cells. Surface and Coatings Technology. 2015;272:415-27.
[19] Jeong H, Roehrens D, Bram M. Facile route for reactive coating of LaCrO3 on high-chromium steels as protective layer for solid oxide fuel cell applications. Materials Letters. 2020;258:126794.
[20] Stange M, Denonville C, Larring Y, Brevet A, Montani A, Sicardy O, et al. Improvement of corrosion properties of porous alloy supports for solid oxide fuel cells. International Journal of Hydrogen Energy. 2017;42:12485-95.
[21] Antepara I, Villarreal I, Rodríguez-Martínez LM, Lecanda N, Castro U, Laresgoiti A. Evaluation of ferritic steels for use as interconnects and porous metal supports in IT-SOFCs. Journal of Power Sources. 2005;151:103-7.
[22] Bautista A, Arahuetes E, Velasco F, Moral C, Calabrés R. Oxidation Behavior of Highly Porous Metallic Components. Oxidation of Metals. 2008;70:267.
[23] Bautista A, Velasco F, Abenojar J. Oxidation resistance of sintered stainless steels: effect of yttria additions. Corrosion Science. 2003;45:1343-54.
[24] Tucker MC. Personal power using metal-supported solid oxide fuel cells operated in a camping stove flame. International Journal of Hydrogen Energy. 2018;43:8991-8.
[25] Tucker MC, Ying AS. Metal-supported solid oxide fuel cells operated in direct-flame configuration. International Journal of Hydrogen Energy. 2017;42:24426-34.
[26] Young DJ, Zurek J, Singheiser L, Quadakkers WJ. Temperature dependence of oxide scale formation on high-Cr ferritic steels in Ar–H2–H2O. Corrosion Science. 2011;53:2131-41.
[27] Zeng Z. Corrosion of metallic interconnects for SOFC in fuel gases. Solid State Ionics. 2004;167:9-16.
[28] Dogdibegovic E, Wang R, Lau GY, Tucker MC. High performance metal-supported solid oxide fuel cells with infiltrated electrodes. Journal of Power Sources. 2019;410-411:91-8.
[29] Dogdibegovic E, Fukuyama Y, Tucker MC. Ethanol internal reforming in solid oxide fuel cells: A path toward high performance metal-supported cells for vehicular applications. Journal of Power Sources. 2020;449:227598.
[30] Falk-Windisch H, Svensson JE, Froitzheim J. The effect of temperature on chromium vaporization and oxide scale growth on interconnect steels for Solid Oxide Fuel Cells. Journal of Power Sources. 2015;287:25-35.
[31] Tucker MC. Durability of symmetric-structured metal-supported solid oxide fuel cells. Journal of Power Sources. 2017;369:6-12.
[32] Rose L. On The Degradation Of Porous Stainless Steel In Low And Intermediate Temperature Solid Oxide Fuel Cell Support Materials: The University of British Columbia, Vancouver; 2011.
[33] Shen F, Wang R, Tucker MC. Long term durability test and post mortem for metal-supported solid oxide electrolysis cells. Journal of Power Sources. 2020;Accepted.
[34] Wang R, Dogdibegovic E, Lau GY, Tucker MC. Metal-Supported Solid Oxide Electrolysis Cell with Significantly Enhanced Catalysis. Energy Technology. 2019;7:1801154.
[35] Żurek J, Wessel E, Niewolak L, Schmitz F, Kern TU, Singheiser L, et al. Anomalous temperature dependence of oxidation kinetics during steam oxidation of ferritic steels in the temperature range 550–650 °C. Corrosion Science. 2004;46:2301-17.

[36] Tucker MC. Progress in Metal-Supported Solid Oxide Electrolysis Cells: A Review. International Journal of Hydrogen Energy. 2020;Accepted.
[37] Wang R, Sun Z, Choi J-P, Basu SN, Stevenson JW, Tucker MC. Ferritic stainless steel interconnects for protonic ceramic electrochemical cell stacks: Oxidation behavior and protective coatings. International Journal of Hydrogen Energy. 2019;44:25297-309.
[38] Boldrin P, Ruiz-Trejo E, Mermelstein J, Bermudez Menendez JM, Rami Rez Reina T, Brandon NP. Strategies for Carbon and Sulfur Tolerant Solid Oxide Fuel Cell Materials, Incorporating Lessons from Heterogeneous Catalysis. Chem Rev. 2016;116:13633-84.
[39] Saunders SRJ, Monteiro M, Rizzo F. The oxidation behaviour of metals and alloys at high temperatures in atmospheres containing water vapour: A review. Progress in Materials Science. 2008;53:775-837.
[40] Young DJ. High Temperature Oxidation and Corrosion of Metals: Elsevier Science; 2008.
[41] Tucker MC, Lau GY, Jacobson CP, DeJonghe LC, Visco SJ. Stability and robustness of metal-supported SOFCs. Journal of Power Sources. 2008;175:447-51.
[42] Yang Z, Xia G, Singh P, Stevenson JW. Effects of water vapor on oxidation behavior of ferritic stainless steels under solid oxide fuel cell interconnect exposure conditions. Solid State Ionics. 2005;176:1495-503.